Monthly Isopycnal/Mixed-layer Ocean Climatology (MIMOC)*

Sunke Schmidtko[1,2], Gregory C. Johnson[1], and John M. Lyman[1,3]

[1]National Oceanic and Atmospheric Administration, Pacific Marine Environmental Laboratory, Seattle, Washington

[2]University of East Anglia, School of Environmental Sciences, Norwich, United Kingdom

[3]Joint Institute for Marine and Atmospheric Research, University of Hawaii at Manoa, Honolulu, Hawaii

submitted to

Journal of Atmospheric and Oceanic Technology

14 February 2012

*Pacific Marine Environmental Laboratory Contribution Number 3805

Corresponding Author: Sunke Schmidtko, School of Environmental Sciences, University of East Anglia, Norwich, NR4 7TJ, UK. Email: s.schmidtko@uea.ac.uk

Abstract

Construction of a monthly, isopycnal/mixed-layer ocean climatology (MIMOC) is explicated, motivated by comparisons with other monthly ocean climatologies. All available quality-controlled profiles of temperature (T) and salinity (S) versus pressure (P) collected by conductivity-temperature-depth (CTD) instruments from the Argo Program, Ice-Tethered Profilers, and archived in the World Ocean Database are used for this climatology. MIMOC includes maps of mixed layer properties (potential temperature (θ), S, and maximum P) as well as maps of interior ocean properties (θ, S, and P) on neutral density surfaces. The final product merges the two onto a pressure grid spanning the upper 1500 dbar of the global ocean. All maps are at monthly × 0.5° × 0.5° resolution. The optimal interpolation used to map the data incorporates an isobath-following component using a "Fast Marching" algorithm, as well as front-sharpening components in both the mixed layer and on interior isopycnals. Recent data are emphasized in the mapping. The goal is to compute a climatology that looks as much as possible like a synoptic survey sampled circa 2005–2010 during any phase of the seasonal cycle, minimizing transient eddy and wave signatures. MIMOC preserves a surface mixed layer, minimizes both diapycnal and isopycnal smoothing of θ–S, as well as preserving density structure in the vertical (pycnoclines and pycnostads) and the horizontal (fronts and their associated currents). It is statically stable by construction and resolves water-mass features, as well as fronts and associated currents, with a high level of detail and fidelity.

1. Introduction

An accurate description of the mean state of the ocean is a long-time goal of oceanographic science. Global- to basin-scale surveys of ocean water properties were initiated over a century ago, with the famous global expedition of the *Challenger* in the 1870s (Murray 1885)followed by the *Fram* expedition towards the North Pole 1893–1896 (Nansen 1900), the *Discovery* expedition to Antarctica 1901–04 (Deacon 1937), the *Meteor* expedition of the South Atlantic 1925-27 (e.g., Wüst and Defant 1936), the extensive Atlantic surveys associated with the International Geophysical Year in 1957–1958 (e.g., Fuglister 1960), the work on the *Eltanin* in the Southern Ocean in the 1960s (e.g., Gordon 1966; Pytowicz 1968), and the global GEOSECs survey during the 1970s (e.g., Bainbridge 1976), to name several.

A recent and comparatively comprehensive milestone in global ocean water property exploration was the one-time hydrographic survey conducted as part of the international World Ocean Circulation Experiment (WOCE) during the 1980s and 1990s (e.g., King et al. 2001). This monumental effort gathered measurements of a number of different water properties with very high accuracy and high vertical and along-track resolution from the ocean surface to its floor, with the global ocean sampled by a grid-like pattern of coast-to-coast tracks. However, the effort, ship-time, and hence expense required for such surveys necessitated gaps between tracks – and seasonal coverage was largely lacking (most of the tracks were only visited once, usually not in winter – only a few hardy scientists elect to work in, for instance, the Labrador Sea in February). Still, this data set affords very useful three-dimensional maps of ocean water properties, and comprises a global baseline of late 20th century ocean conditions.

The Argo Program, with more than 3000 active, fully autonomous profiling floats each collecting and reporting a CTD (conductivity-temperature-depth instrument) profile between the surface and a target pressure of 2000 dbar, nominally every 10 days, provides high-quality, spatially and temporally distributed sampling of temperature and salinity in the global ice-free ocean (Roemmich et al. 2009). This program started in 2000, first achieved sparse global coverage by around 2004 or 2005, and reached its 3000 active float target in late 2007. Floats also now sample under seasonal sea ice (Klatt et al. 2007), and ice-tethered profilers (ITPs) provide data under perennial sea ice (in the Arctic; Toole et al. 2011). This near-global, year-round, high-quality sampling of the upper half of the ocean volume for both temperature and salinity is revolutionary for observational physical oceanography.

As oceanographic data have become more plentiful and better resolved, more ocean climatologies and atlases have been constructed (e.g., Table 1). We compare our results to three isobar-averaged global (or near-global) and monthly products: the World Ocean Atlas 2009 (Locarnini et al. 2010; Antonov et al. 2010; hereafter WOA09), the 2009 CSIRO Atlas of the Regional Seas (Ridgway et al. 2002; hereafter CARS09), and the Argo-based Marine Atlas (Roemmich and Gilson 2009; hereafter AMA). WOA09 is a monthly atlas mapped on isobars. CARS09, also an isobaric atlas, provides a mean, annual, and semiannual harmonics, takes topography into account, and uses adaptive smoothing scales. Both WOA09 and CARS09 use all available data to estimate a mean seasonal cycle. Because of the irregular sampling of oceanographic data in the past, they can be termed mixed-era climatologies. AMA uses Argo data only, and has monthly maps for individual years starting in January 2004. Since the climatology presented here

also represents the mean seasonal cycle, for AMA we average all the years for a given month prior to comparisons. Climatologies averaged on isopycnals also exist, but one is for the mean only (Gouretski and Koltermann 2004; hereafter WGHC) and another is really a dataset and software tools (Lozier et al. 1995; Curry 1996; hereafter Hydrobase). Hence we do not compare our results to these last two products.

Here we construct a Monthly Isopycnal/Mixed-layer Ocean Climatology (MIMOC) that combines different features of previous efforts and adds a few new features (Table 1). The interior ocean properties are mapped on isopycnals, much like WGHC and Hydrobase. However, we also map surface mixed layer properties and merge those maps with those of the interior properties onto a regular pressure grid. We respect the topography, somewhat like CARS09, but using a different algorithm, and add an equatorial barrier to smoothing. We also include front-sharpening weighting schemes within the ocean interior and in the mixed layer. Finally, we focus on the best-sampled era, 2005–2010, where possible, supplemented by historical CTD data. Historical data are given a lower signal-to-noise ratio to discount them where sufficient recent data exist but to allow their use in the maps where recent data are sparse, especially in some marginal seas, at high latitudes, and near the coasts (including on continental shelves).

Immediately following this introduction, the data are discussed. Subsequently the methods used to generate MIMOC are presented first in summary, and then individually – motivated by targeted comparisons with other climatologies. After this presentation, we discuss one area that could still benefit from improvement – joining the mixed layer to the interior isopycnals in regions of strong gradients. Conclusions follow.

2. Data

This climatology uses CTD profiles from three sources: Argo floats (e.g. Roemmich et al. 2009), Ice Tethered Profilers (ITPs; Toole et al. 2011), and shipboard data from World Ocean Database 2009 (Boyer et al. 2009; hereafter WOD). Except in a few isolated regions, Argo CTD data are the main data contributor in the open ocean and ITPs are contemporaneous contributors in the Arctic (compare Fig. 1b and 1c). Since Argo does not yet sample continental shelves, some marginal seas, or most ice-covered regions, attempts to map the global oceans must include shipboard data. Since the sampling periods of shipboard compared to Argo and ITPs are vastly different (Fig, 1a), temporal sampling bias in mapping shelf regions and some marginal seas vs. the open oceans is unavoidable.

All Argo float profiles from an Argo global data assembly center as of February 2011 that have a QC flag 2 or better are used, employing adjusted (delayed-mode) variables as available (> 566,000 profiles, Fig. 1a, 1b). WOD profiles available as of January 2011 are used if quality flags are 0 or 2, profiles have monotonically increasing pressure, at least 20 vertical measurements spaced less than 12 dbar apart, and the maximum pressure is larger than the shallower of 200 dbar from the bottom or 1500 dbar (> 415,000 profiles, Fig. 1a, c). Bathymetry data used for this quality control step and within the mapping process in the following is the ETOPO1 dataset (Amante and Eakins, 2009). ITP profiles processed to Level 2 or better available as of May 2011 are used (> 24,000 profiles). The median parameters on each mapping surface are used for each week of ITP data from one instrument, to reduce the number of profiles, which are collected at higher than daily frequency. No further quality control is applied to ITP data,

since this data set is very well quality controlled, hence clean. In all instances, temperature (T) and salinity (S) must both be available at a given reported pressure (P, or depth) level to be included (ITP profiles are included with the Argo float data in Fig. 1).

While this basic, initial data screening benefits from the efforts of groups involved with WOD, Argo, and ITP, it might be deemed minimal compared the rigorous, labor-intensive visual quality control effort applied to the datasets for some climatologies. Our quality control relies instead on a robust mapping algorithm including the removal of outliers via statistical filters and automatic down-weighting of data points with unusual water-mass properties that pass through these filters.

3. Methods: Constructing the climatology

The process of constructing MIMOC is fairly involved, so we outline it here before delving into detail. First, the profiles are prepared, with water properties derived and interpolated onto isopycnal surfaces. Properties of the mixed layer are determined. Then data near each gridpoint are selected and outliers are found and discarded. Nearness to the grid-point includes consideration of fronts (data on the other sides of fronts are considered farther away) and bathymetry (along-isobath distances are considered closer than across-isobath distances using a fast-marching algorithm, and land barriers are respected). Mean properties weighted by nearness are generated as a first guess prior to objective mapping. Pre-2007 data are de-emphasized in the objective maps by increasing their noise-to-signal energy in the mapping. Objective maps of water properties in the mixed layer and on isopycnals in the ocean interior are generated. These maps are lightly low-pass filtered and gaps are filled. Spice-preserving adjustments are made to θ and S

to compensate for effects of artificial mixing (smoothing) in the presence of a non-linear equation of state. Finally the mixed layer and interior isopycnal maps are merged onto a set of standard pressures.

Profile preparation

For each individual profile, θ is calculated using the 1980 equation of state and neutral density (γ_n) using the approximation of McDougall and Jackett (2005). The mixed layer S, θ, γ_n, and depth (hereafter *MLP*; since pressure is used here as the vertical coordinate) are computed using the Holte and Talley (2009) algorithm. If the algorithm fails to provide a *MLP* (e.g., when $P > 20$ dbar for the shallowest measurement) the profile is removed from the data set.

Only profiles with density inversions < 0.06 kg m^{-3} between two vertically adjacent measurements are used. These very small density inversions are tolerable and assumed to originate from measurement inaccuracies or truncation errors. They are circumvented by re-ordering raw profiles by density.

Following these steps, S, θ, and P for each profile are linearly interpolated vertically onto 352 fixed γ_n surfaces, eschewing extrapolation. The surfaces chosen are a compromise between reasonable computation time and file sizes versus adequate vertical resolution throughout the global ocean and marginal seas, with their large regional variations in vertical distribution of γ_n. The lightest 60 surfaces are logarithmically spaced from $7.91 \leq \gamma_n \leq 15.64$ kg m^{-3}. The next 263 surfaces are roughly logarithmically spaced from $15.64 \leq \gamma_n \leq 28.56$ kg m^{-3}. The densest 29 surfaces are distributed in 3 linear subsets with decreasing γ_n intervals from $28.57 \leq \gamma_n \leq 29.08$ kg m^{-3} to span the dense waters in the Nordic and Mediterranean seas.

Data selection and objective mapping

All objective maps are global and made at monthly × 0.5° × 0.5° resolution. The objective mapping procedure used is fairly standard (e.g., Bretherton et al. 1976), but with three innovations, each explained in subsections that follow. One innovation is the use of a fast-marching algorithm to transform distance coordinates based on the bottom topography and the presence of the equator, reducing smoothing across isobaths and the equator, and preventing smoothing across land. This innovation is foreshadowed immediately below by the term "along-pathway distance". A second innovation is additions to the weighting and covariance functions that sharpen fronts in both the mixed layer and the ocean interior, also explained later. A third innovation is an addition to the diagonal of the covariance matrix that de-emphasizes data prior to 2007 in the objective maps. For the mixed layer we map γ_n, θ, S, MLP, year values, and a formal error. In the interior we map θ, S, P, γ_n, year, and formal error. In addition, weighted means are also generated iteratively, as described below, for all these quantities. These weighted means are used as first-guesses for the objective maps and are comparatively smooth. They may be useful for work that requires that characteristic.

The closest 1800 profiles within 2000 km of the along-path distance from each gridpoint (regardless of month) are used for mapping at that gridpoint. If there are less than 1800 profiles in this radius, then all are used, but data from more than 10 profiles must be found to attempt a map for a gridpoint. The initial weighting function (accounting for along-path distance and time of the year) is assigned a fairly conventional Gaussian form:

$$w_i = e^{-\left(\left(\frac{\Delta t}{L_t}\right)^2 + \left(\frac{\Delta d_x}{L_x}\right)^2\right)}, \quad (1)$$

where Δt is the temporal difference between the month being mapped and that of the data value (circular, disregarding the year), L_t the temporal decorrelation scale of 45 days, Δd the along-path distance between the gridpoint and the data sample, and L_d the lateral decorrelation scale of 330 km.

For each month the 300 profiles with the highest weights and 50 more random profiles from the next highest-weighted 900 profiles are selected from the 1800 points mentioned above. A floor of $\varepsilon = 10^{-6}$ is set for a new, modified weighting function, $\boldsymbol{W}_i = \boldsymbol{w}_i \cdot (1 - \varepsilon) + \varepsilon$. This floor mitigates problems that arise from rounding errors.

Removing outliers

Prior to computing the maps we discard outliers using an interquartile range (IQR) filter. The IQR is simply the third minus the first quartile. Here outliers are defined as being more than two times the IQR below the first quartile or more than two times the IQR above the third quartile. This cut-off is analagous to retaining data within 4 standard deviations, or > 99.9% of the data, for a normal distribution. In the mixed layer this filter is applied to γ_n and MLP values. On interior isopycnals this filter is applied to P and S. Since S and θ are very highly correlated on isopycnals, application of the filter to θ would be redundant.

Sharpening fronts and downweighting remaining outliers

One modification to the weighting and covariance functions prior to mapping the data is designed to sharpen fronts. For the mixed layer the weighted standard deviation for γ_n of

the closest 150 profiles, σ_γ, is computed and used in a term added to the weighting and covariance functions so

$$\omega_i = e^{-\left(\left(\frac{\Delta t}{L_t}\right)^2+\left(\frac{\Delta d_x}{L_x}\right)^2+\left(\frac{\Delta \gamma}{1.2\cdot\sigma_\gamma}\right)^2\right)}, \quad (2)$$

where $\Delta\gamma$ is the difference between the each observed γ_n and the locally weighted mean γ_n calculated using the weight vector $\boldsymbol{W}$ with the weights $\boldsymbol{W}_i$. As above, a floor of 10^{-6} is set for all elements of $\boldsymbol{\omega}_i$ and the result is used to compute a local weighted mean at each gridpoint for all of the properties to be mapped (including γ_n). The effect of this algorithm is to sharpen density fronts in the mixed layer. The factor of 1.2 is chosen to optimize the results based on visual examination of test cases. The new local weighted mean in density is used again in the above equation for $\boldsymbol{\omega_i}$ to compute the final set of weights.

The advantage of using γ_n rather than θ or S for front sharpening in the mixed layer is that lateral distributions of θ and S tend to compensate each other in terms of their contribution to γ_n within the mixed layer in many ocean regions (e.g., Rudnick and Ferrari 1999). Therefore dynamically (rather than thermodynamically) formed fronts within the mixed layer are often best characterized by strong γ_n gradients, rather than those in θ or S. Furthermore, *MLP* is not suitable for mixed-layer front detection since it often exhibits very large and non-normal variability on short temporal and spatial scales.

On γ_n surfaces, we use P for the front-sharpening parameter. Again, this is a dynamical front detector, sensitive to the large vertical excursions of P on γ_n across strong currents like the Gulf Stream, Kuroshio Extension, and Antarctic Circumpolar Current. This modification to the weighting and covariance functions tends to sharpen θ,

S, and *P* gradients across these fronts, suppressing artificial mixing of water masses, and making the mapped fields look more like a synoptic survey, which would see sharp fronts and strong currents. Furthermore, using *P* for front-sharpening on γ_n surfaces reduces the weight of any erroneous measurement in θ, *S*, or *P*. The resulting strong interior gradients are clear from meridional sections (e.g., in the western South Atlantic, Fig. 2) crossing the Antarctic Circumpolar Current (here near 50°S) and the subtropical front (near 40°S). In these locations, especially at the subtropical front, the meridional water property gradients in each of the other climatologies are much smoother than those in MIMOC, resulting in dipoles of water property anomalies of these climatologies with respect to MIMOC, especially pronounced at mid-depth, from 200–600 dbar around the subtropical front. Synoptic meridional sections in this region (e.g., Fig. 2a, b; Tsuchiya et al. 1994) look much more like MIMOC in the strength of these fronts than do the other climatologies, except the synoptic sections also contain prominent eddies that MIMOC does not retain.

Covariance matrix and de-emphasizing pre-2007 data

In addition to providing weighted means that are used as the first guess for the objective maps, the equations above are used to construct the covariance matrices for the objective maps:

$$E_{ij} = e^{-\left(\left(\frac{\Delta t}{L_t}\right)^2+\left(\frac{\Delta d_x}{L_x}\right)^2+\left(\frac{\Delta \gamma}{1.2\cdot\sigma_\gamma}\right)^2\right)}. \qquad (3)$$

The form for the mixed layer is given in (3). On isopycnals the last term in (3) would be instead be $\left(|\Delta P|/\left[1.2\cdot\sigma_P\right]\right)^2$. The difference between the weighting and the covariance

matrices is that in the former the numerators of the three terms in the Gaussian are the differences between each parameter and the grid-point time, location, and weighted mean front-sharpening parameter (γ_n for the mixed layer and P for γ_n surfaces in the ocean interior). For the latter the numerators are the difference in each parameter between the profiles i and j.

An estimate of noise-to-signal ratio is typically added to the diagonal of the covariance matrix prior to objective mapping. Here we use the form:

$$E_{ii} = E_{ii} + \kappa_0 + \kappa_{decade} \cdot (1 - e^{-(\frac{\Delta yr}{\tau})^2}), \tag{4}$$

where E_{ii} is the diagonal of the covariance matrix $\boldsymbol{E}$ and κ_0 is a constant noise-signal ratio, set here to 1.5 (this value chosen, again, by visual evaluation of test cases). Our innovation is to use the noise to de-emphasize pre-2007 data in the objective maps**.** Here κ_{decade} is set to 8.5 years and Δyr is the number of years prior to 1 January 2007 for each data point. After that date Δyr is set to 0. The decadal time-scale τ is set to 12 years. This formulation for the noise ensures that the objective maps are for modern conditions wherever modern data are available. However, the weighted means (which are used as the first-guess for the map and to which the map relaxes in data-sparse regions) are a mixed-era average that includes historical CTD data (dating back to 1970).

The influence of a modern climatology is apparent in areas which have undergone changes in water-mass properties in recent decades, like the warming and shoaling of intermediate water masses (e.g., Schmidtko and Johnson 2012). Weighting historical data in MIMOC less than in climatologies like CARS09 or WOA09 leads to warmer temperatures at 500 dbar in MIMOC, especially in areas with abundant historic profiles,

since MIMOC represents the modern state of the ocean rather than that of prior decades (Fig. 1b–c; 3c–d). AMA on the other hand, using only Argo data after 2004, is as warm or even warmer than MIMOC (Fig. 3b). Shelf regions and high latitude regions with no ITP data lack the amount of recent data provided in the open ocean by the Argo project, thus are more representative of the state of the ocean before 2000 in MIMOC.

At this point objective interpolation, also known as optimal interpolation, objective mapping or objective analysis, $b = \boldsymbol{\omega} \cdot \boldsymbol{E}^{-1} \cdot \boldsymbol{\psi}$, is performed on the anomalies of each parameter from its weighted mean. Here $\boldsymbol{\psi}$ is the vector of residuals of the measured properties and the weighted means, and b is the objectively mapped anomaly. Values of the mapped properties are computed by adding the weighted means to the objectively mapped anomalies *b*. Formal errors are also estimated for the objective maps.

Fast-Marching: Taking bathymetry and the equator into account

In the ocean near-conservation of potential vorticity (e.g., Pedlosky 1987) means that along-isobath decorrelation scales are much longer than cross-isobath ones, and especially in low latitudes, zonal decorrelation scales are much longer than meridional ones. Ocean currents also respect coastlines, with no flow into land. We construct an along-pathway distance to reflect the above constraints using the fast marching method (Sethian 1996; 1999), which is based on Dijkstra's (1959) algorithm. This method is often described in terms of wave-front propagation, as it solves the boundary value problem of the Eikonal equation, $SM_i \left| \nabla t_i \right| = 1$, where *t* is the time and SM_i is the speed at each location in the normal direction of propagation. *SM* will be hereafter called the speed map. Here it is defined between 0 and 1 and represents the fraction of normal

propagation speed. Thus 0 effectively halts wave-front propagation at a gridpoint and 1 allows normal speed wave-front propagation through a gridpoint.

However, here we are really more interested in adjusting distances, so the time to reach gridpoints from the origin, the gridpoint being mapped, is here re-interpreted as distance. We determine a spatially varying speed map for each gridpoint being mapped with the form:

$$SM_i = \left(1 - \left|\log\left(\frac{H_0}{H_i}\right)\right|\right) \cdot e^{\left(\left|\frac{\vartheta_0 - \vartheta_i}{e^{\frac{\vartheta_0}{7.5}}}\right|\right)}, \tag{5}$$

where H_0 is the water depth at the gridpoint being mapped, H_i are the water depths in nearby grid boxes i in which data points might be located, ϑ_0 is the latitude of the gridpoint being mapped, and ϑ_i are the latitudes of nearby grid boxes i. The depth for each gridpoint is determined by the median of all depths within the area of the grid box in the ETOPO1 dataset. If more than 10% of the area associated with a grid box is above the surface, the whole gridpoint is treated as land to ensure narrow passages are closed to the mapping.

The speed map is unity in locations that have the identical depth and same latitude as the gridpoint to be mapped. The logarithmic term in (5) reduces the traveling speed through grid boxes with significant differences in water depth from the gridpoint being mapped. The exponential term reduces the speed through grid boxes that are at different latitudes than any gridpoint being mapped. The closer to the equator the gridpoint being mapped, the stronger is this effect. Thus the first term creates a longer along-path distance than the Cartesian one for cross-isobath mapping, while the second term creates a longer distance than the Cartesian one for meridional mapping, more anisotropic nearer

the equator. We set a floor of $SM_i = 0.1$ for any water-covered area, a maximum tenfold increase in path distance. However, $SM = 0$ for gridpoints marked as land to prevent mapping pathways from crossing land. Hence fast marching eliminates the necessity to define 'hand drawn' boundaries for mapping around peninsulas, basin boundaries, bays and such.

The fast-marching algorithm does not retain the second dimension, but that information is necessary for representing property gradients for the objective mapping. For this purpose we apply a pathfinding algorithm to the distance maps to determine the angles at which pathways leave the gridpoint being mapped in order to reach each grid box via the minimum fast-marching distance.

The effectiveness of fast marching in separating ocean interior from shelf waters is well illustrated in the Bering Sea (Fig. 4), where the Bering Slope Current (e.g., Johnson et al. 2004) is associated with a front between the interior ocean and the Bering Shelf. Here MIMOC (Fig. 4a, b) exhibits a distinct separation of cold, fresh shelf waters and warmer, saltier waters offshore that is blurred in some other climatologies (Fig. 4c–f). Also, in the southern half of the Bering Shelf, just as in synoptic sections (e.g., Coachman 1986), MIMOC has the strongest S gradient located right at the shelf break, and the strongest θ gradient slightly northeast (landward) of the shelf break.

Post-mapping – smoothing and infill.

Mapped values at grid points with weight $< 10^{-6}$ are removed after mapping to eliminate any remaining artifacts associated from round-off errors. After discarding these points from the maps, water properties in the mixed layer and on each interior ocean isopycnal surface are smoothed with a two-dimensional 5^{th}-order binomial filter to reduce small-

scale noise likely owing to the fast-marching algorithm. Water properties are also interpolated onto missing gridpoints with a spatial 3rd-order binomial filter to fill in areas like small inlets that are excluded during the mapping process due to the difficulty of applying fast-marching in these areas. This interpolation is performed iteratively, always mapping locations with a maximum of adjacent gridpoints first.

Cabbeling and thermobaricity biases

Because of the non-linearity of the equation of state, waters of the same density and pressure but different θ and S (warmer-saltier versus colder-fresher) will always become slightly denser when mixed, a process called cabbeling (McDougall 1987). In addition, mixing waters of the same density but different θ, S, and P also results in a change of density which can be positive or negative, a process called thermobaricity (McDougall 1987). Both processes can create biases in density when mapping, because mapping explicitly smoothes (hence artificially mixes) θ and S (and on isopycnals, P) data (e.g., Gille 2004). The result is that densities are greater (and sea level lower) when they are computed from mapped values rather than mapped themselves.

The MIMOC fast-marching and front-sharpening algorithms minimize smoothing of distinct water-masses, but smoothing is part of constructing a climatology, and in regions of strong fronts, the non-linear biases become noticeable. They are especially apparent when mapping on isopycnals because the density calculated from mapped θ and S values on an isopycnal is different (usually denser) than the initial isopycnal, especially in regions of strong θ–S gradients (Fig. 5).

There are two possible responses to this problem: One can choose to conserve θ and S and accept any (largely localized) increase in density, or one can adjust the

mapped θ and S values so they lie back on the initial isopycnal and conserve density. While conservation arguments support the former course, this is an isopycnal climatology, so we choose the latter. We further choose to conserve spiciness (e.g.. Flament 2002) in our adjustment, meaning that we make the water properties warmer and fresher in amounts so that the θ and S changes contribute equally in terms of their contributions to density for the return to the initial isopycnal. Thus additive adjustments $\Delta\theta$ and ΔS are given by

$$\Delta\theta = \frac{\gamma(S_{map},\theta_{map}) - \gamma_i}{2\alpha\rho_0} \text{ and } \Delta S = \frac{\gamma(S_{map},\theta_{map}) - \gamma_i}{2\beta\rho_0}, \quad (6)$$

where γ_i is the initial isopycnal, θ_{map} and S_{map} the properties mapped, α the local thermal expansion coefficient, and β the local haline contraction coefficient (Fig. 5). The adjustments are everywhere sufficiently small that the local tangent to density (lines of constant spice) can be linearized. To be consistent we make similar adjustments to θ and S for the mixed layer maps, using the mapped mixed layer density as a target for the adjustments.

Some of the strongest non-linear mixing biases found are in the western boundary currents and their extensions – where the warm salty waters of the subtropical gyres collide with the waters of the colder and fresher subpolar gyres. The North Atlantic Current is an extreme example (Fig. 6). Even in the highest gradient regions of the upper reaches of this current between the gyres the adjustments only reach about +0.3 °C for θ and about -0.09 for S (up to +0.5 °C and -0.15 PSS-78 on just three gridpoints). If these biases were left in density, isopycnals in the core of the current would artificially shift about 20 km northward in the upper 80 dbar of this same region. More generally these

biases are quite small. The median correction for θ is 4.3×10^{-4} °C on isopycnals. The median correction for θ in the mixed layer (6.7×10^{-4} °C) is only slightly larger.

Back to pressure co-ordinates: Connecting the mixed layer and interior isopycnals.

Monthly maps of water properties in the mixed layer and on interior ocean isopycnals are products in their own right, but we also combine them onto a regular pressure grid for increased ease of use. This re-gridding is done at each geographical grid-point and for each month. Mixed layer properties are assigned to all pressure grid-points shallower than the local *MLP*. The *MLP* and interior ocean pressures at least 5dbar greater than the *MLP* and lower than the maximum possible bottom pressure are used to put θ and S on a regular pressure grid via linear interpolation.

4. Discussion and an unresolved issue

One advantage of isobaric mapping is that it is simple and can be performed over the whole water column. In contrast, isopycnal mapping requires the separate computation of the mixed layer, or a surface isobaric layer, for the reasons detailed below. This calculation can either be done by isobaric mapping down to a depth generally below the seasonal thermocline as done in WGHC, or by merging an individually mapped mixed layer to the interior ocean isopycnal maps, as done here. Otherwise, the isosopycnal/mixed-layer formulation has some very strong advantages over a simple isobaric mapping, and the additions of front-sharpening and bathymetry-respecting algorithms add to those advantages. However, there are always trade-offs in constructing a climatology. One difficulty – biases in density resulting from artificial cabbeling (and thermobaricity) owing to smoothing during the mapping process – has been discussed

and dealt with above. In fact, that issue is probably larger, and unaddressed, in most isobaric climatologies. A remaining unresolved issue, the difficulty of mapping near regions where isopycnals outcrop, is discussed at the end of this section.

Mixed layer

A mixed layer is often a desirable feature in a climatology. The mixed layer is the part of the water column in direct contact with the atmosphere and water properties are by definitition (in the ocean and in MIMOC, e.g., Fig. 7) homogeneous within the mixed layer. Resolving the seasonal cycle in the mixed layer, including dense, deep winter mixed layers, is crucial to water mass formation (e.g. Stommel 1979). Thus resolving the mixed layer and its temporal evolution in a climatology better allows study of water mass formation using that climatology. For example, the evolution of a deep winter mixed layer is clear in MIMOC (Fig. 7) within the formation regions for the South East Pacific Subtropical Mode Water (SEPSTMW) at 20.5 °S and 99.5 °W, as expected from analyses of synoptic data (e.g., Wong and Johnson 2003), but is less obvious in other climatologies (Fig. 7). The mixed layer is also clear in vertical sections from synoptic data and MIMOC, but again less clearly defined in other climatologies (Fig. 2).

Isopycnal mapping

Isopycnal maps better follow water parcels both laterally and vertically. One advantage of this tendency over isobaric maps is limiting the creation of artificial water masses found in climatologies smoothed on isobars (e.g., Lozier et al. 1994). However, the smoothing effects on vertical density gradients by transient vertical excursions of

isopycnals owing to planetary waves, internal waves, and tides are also greatly reduced in isopycnal maps relative to isobaric maps.

For example, the strong and shallow pycnocline in the eastern equatorial Pacific undergoes substantial excursions owing to the seasonal cycle (e.g., Johnson et al. 2002), but also from Kelvin waves, Rossby waves, and ENSO (e.g., McPhaden and Yu 1999). In an isobaric average these vertical excursions of isopycnals (along with those owing to eddies, internal waves, and tides) will tend to smear out the pycnocline in the vertical and reduce its magnitude substantially from what would be observed in a synoptic survey, as well as reducing the magnitude of θ–S features within the pycnocline. As a result, MIMOC exhibits a much stronger and sharper pycnocline in this region than do other climatologies (as visualized by the squared Brunt-Väisälä frequency – N^2; Fig. 8, right panels), and much better preserves the South Pacific salinity maximum and North Pacific salinity minimum that meet within the pycnocline at the equator (Fig. 8, left panels; Johnson and McPhaden 2002).

Isopycnal boundary problems

The aforementioned unresolved issue with isopycnal mapping is that mapping errors which increase near the boundaries of the domain, where data are only available on one side of the mapped gridpoint, occur not only near coastlines and at the edges of data-sparse regions as they do for other maps, but also anywhere (or anytime) that the isopycnal outcrops in the ocean interior. On the other hand, the mixed layer (and any isobaric) maps do not have this source of uncertainty (and bias) in the ocean interior.

Biases from this isopycnal mapping uncertainty should be most noticeable where the mixed layer meets interior ocean isopycnals in regions with large surface density

gradients and limited data availability, for instance in the Antarctic Circumpolar Current (Fig. 9). The temperature inversion visible in MIMOC just below the mixed layer here may occur at least in part because the mixed layer map is constrained by both the colder, fresher water to the south and the warmer saltier water to the north, whereas the isopycnal maps near their surface outcrops see only the warmer, saltier water to the north of the outcrop. Thus, the isopycnal maps may be biased towards those northern warm salty values, potentially creating the temperature inversion just below the mixed layer visible here, or small discontinuities between the mixed layer and the ocean interior seen in other locations. However, this specific feature may also realistic; some of the raw profiles in the region do display a temperature inversion similar to that found in the maps.

A similar problem is found on dense isopycnals near 1800–2000 dbar, where the majority of data profiles used here end. In this instance the densest isopycnals are observed by Argo only when they are shallower than average, whereas slightly lighter isopycnals are observed for their entire pressure range. Hence, the densest isopycnals are biased towards shallow pressures in the maps, creating artificially strong stratification just above 2000 dbar. For this reason MIMOC is only published up to 1500 dbar where this problem does not exist. To include the deeper oceans, MIMOC would need to be recomputed with full-depth CTD profiles only and then merged to the upper ocean climatology. While we plan to effect this improvement, it is not a simple task, because a new problem of temporal discontinuities in full depth and upper ocean sampling arises.

5. Summary

MIMOC is a monthly isopycnal/mixed-layer ocean climatology. The primary product from MIMOC is climatological monthly maps of water properties (S and θ) on a regular pressure grid. The numbers of weighted observations for the maps and the mapped dates are provided for the maps on the pressure grid. Mapped mixed layer properties (S, θ, and *MLP)* and water properties (S, θ, and P) on select neutral density surfaces are also available. Numbers of weighted observations for the maps, the mapped dates, and formal mapping errors are provided for the mixed layer and isopycnal maps. Smoother weighted mean fields are also provided on the pressure grid, for the mixed layer, and on the selected neutral density surfaces.

The goal of MIMOC is to make maps that preserve many of the features observed in a synoptic survey, but minimizing the influences of eddies, planetary waves, internal waves and tides, and other transient phenomena. MIMOC preserves water-mass properties both vertically and laterally; resolves boundary currents and shelf regimes (where data are available) while observing natural boundaries like land, inlets, islands, and ridges; accounts for the short meridional scales of the equatorial current system; retains true mixed layers as well as preserving strong, sharp pycnoclines; and is stably stratified.

To accomplish these goals MIMOC uses mapping mechanisms including combining mixed layer and interior isopycnal maps, employing front-sharpening algorithms that down-weight profiles with regionally atypical characteristics, and a “Fast Marching” algorithm that accounts for the influences of bathymetry and latitude (especially near the equator) on water-property distributions. Comparing MIMOC in

detail to other widely used climatologies suggests that MIMOC fulfills the goals listed above as well as or better than any of the comparison products.

Isopycnal maps are uncertain, and perhaps even biased, near their surface outcrops, so joining the ocean interior to the surface mixed layer in MIMOC is not free from biases, especially in regions of large surface density gradients and sparse data distributions. This mismatch may result in small temperature inversions or other discontinuities, but the maps are stably stratified by construction.

MIMOC could not be constructed without a high-quality, temporally and spatially well-sampled set of profiles of contemporaneously measured temperature and salinity – Argo. Improvements could include extending MIMOC to the deep ocean, adding data in remote regions, mapping water-mass properties additional to θ and S, and developing a method for better matching mixed layer and isopycnal properties at outcrop locations.

Acknowledgments. We thank all those who participated in the collection, calibration, and assembly of the shipboard (http://www.nodc.noaa.gov/OC5/WOD09/pr_wod09.html), Argo, and ITP CTD data used here. The Ice-Tethered Profiler data were collected and made available by the Ice-Tethered Profiler Program based at the Woods Hole Oceanographic Institution (http://www.whoi.edu/itp). Argo float profile data were collected and made freely available by the International Argo Project and the national programs that contribute to it (http://www.argo.ucsd.edu). This work was supported by the NOAA Climate Program Office and NOAA Research.

References

Amante, C., and B. W. Eakins, 2009: *ETOPO1 1 Arc-Minute Global Relief Model: Procedures, Data Sources and Analysis*. NOAA Technical Memorandum NESDIS NGDC-24, U.S. Government Printing Office, Washington, D.C., 19 pp.

Antonov, J. I., D. Seidov, T. P. Boyer, R. A. Locarnini, A. V. Mishonov, H. E. Garcia, O. K. Baranova, M. M. Zweng, and D. R. Johnson, 2010: *World Ocean Atlas 2009, Volume 2: Salinity*. S. Levitus, Ed. NOAA Atlas NESDIS 69, U.S. Government Printing Office, Washington, D.C., 184 pp.

Bainbridge , A. E., 1976: GEOSECS Atlantic Expedition. Sponsored by International Decade of Ocean Exploration, National Science Foundation, U.S. Government Printing Office, Washington, D.C.

Boyer, T. P., J. I. Antonov , O. K. Baranova, H. E. Garcia, D. R. Johnson, R. A. Locarnini, A. V. Mishonov, T. D. O'Brien, D. Seidov, I. V. Smolyar, and M. M. Zweng, 2009: *World Ocean Database 2009.* S. Levitus, Ed., NOAA Atlas NESDIS 66, U.S. Gov. Printing Office, Wash., D.C., 216 pp., DVDs. 2

Bretherton, F., R. Davis, and C. Fandry, 1976: A technique for objective analysis and design of oceanographic experiments applied to MODE-73, *Deep-Sea Res.*, **23**, 559–582, doi:10.1016/0011-7471(76)90001-2.

Coachman, L. K., 1986: Circulation, water masses, and fluxes on the southeastern Bering Sea Shelf. *Cont. Shelf Res.*, **5**, 23–108.

Curry, R. G., 1996, HydroBase: A database of hydrographic station and tools for climatologic analysis. WHOI Technical Report 96-01, 55 pp.

Deacon, G. E. R., 1937: The hydrology of the southern ocean. *Discovery Reports*, **15**, 124 pp.

Dijkstra, E. W., 1959: A note on two problems in connexion with graphs. *Numerische Mathematik*, **1**, 269–271. doi:10.1007/BF0138639.

Flament, P., 2002: A state variable for characterizing water masses and their diffusive stability: spiciness. *Prog. Oceanogr.*, **54**, 493–501.

Fuglister, F. C., 1960: *Atlantic Ocean Atlas of Temperature and Salinity Profiles and Data from the International Geophysical Year of 1957–1958*. Woods Hole Oceanographic Institution Atlas Series, Volume **1**, Woods Hole, Massachusetts, 209 pp.

Gille, S. T., 2004: How nonlinearities in the equation of state of seawater can confound estimates of steric sea level change, *J. Geophys. Res.*, **109**, C03005, doi:10.1029/2003JC002012.

Gordon, A. L., 1966: Potential temperature, oxygen and circulation of bottom water in the Southern Ocean. *Deep-Sea Res.*, **13**, 6, 1125–1138, doi:10.1016/0011-7471(66)90704-2.

Gouretski, V., and Koltermann, K., 2004: WOCE Global Hydrographic Climatology, *Berichte des BSH*, **35**, 52 pp., ISSN: 0946-6010.

Holte, J., and L. Talley, 2009. A new algorithm for finding mixed layer depths with applications to Argo data and Subantarctic Mode Water formation. *J. Atm. Oceanic Tech.*, **26**, 1920–1939, doi:10.1175/2009JTECHO543.1.

Johnson, G. C., and S. C. Doney. 2006: Recent western South Atlantic bottom water warming. *Geophys. Res. Lett.*, **33**, L14614, doi:10.1029/2006GL026769

Johnson, G. C., and M. J. McPhaden, 1999: Interior pycnocline flow from the subtropical to the equatorial Pacific Ocean. *J. Phys. Oceanogr.*, **29**, 3073–3089, doi:10.1175/1520-0485(1999)029<3073:IPFFTS>2.0.CO;2.

Johnson, G. C., B. M. Sloyan, W. S. Kessler, and K. E. McTaggart, 2002: Direct measurements of upper ocean currents and water properties across the tropical Pacific Ocean during the 1990's. *Prog. Oceanogr.* **52**, 31–61, doi:10.1016/S0079-6611(02)00021-6.

Johnson, G. C., P. J. Stabeno, and S. D. Riser, 2004: The Bering Slope Current System revisited. *J. Phys. Oceanogr.*, **34**, 384–398, doi:10.1175/1520-0485(2004)034<0384:TBSCSR>2.0.CO;2.

King, B. A., E. Firing, and T. M. Joyce, 2001: *Shipboard Observations during WOCE* in *Ocean Circulation and Climate: Observing and Modelling the Global Ocean*. G. Siedler, J. Church, and J. Gould, Eds., International Geophysics, Volume **77**, Academic Press, 99–122.

Klatt, O., O. Boebel, and E. Fahrbach, 2007: A profiling float's sense of ice. *J. Atmos. Oceanic Tech.,* **24**, 1301–1308.

Locarnini, R. A., A. V. Mishonov, J. I. Antonov, T. P. Boyer, H. E. Garcia, O. K. Baranova, M. M. Zweng, and D. R. Johnson, 2010: *World Ocean Atlas 2009, Volume 1: Temperature*. S. Levitus, Ed. NOAA Atlas NESDIS 68, U.S. Government Printing Office, Washington, D.C., 184 pp.

Lozier, M. S., M. S. McCartney and W. B. Owens, 1994: Anomalous anomalies in averaged hydrographic data. *J. Phys. Oceanogr.*, **24**, 2624–2638.

Lozier, M. S., W. B. Owens, and R. G. Curry, 1995. The climatology of the North Atlantic. *Prog. Oceanogr*. **36**, 1–44.

McDougall, T. J., 1987: Thermobaricity, cabbeling, and water-mass conversion, *J. Geophys. Res.*, **92**, 5448–5464, doi:10.1029/JC092iC05p05448.

McDougall, T. J., and D. R. Jackett, 2005: The material derivative of neutral density, *J. Mar. Res.*, **63**, 159–185.

McPhaden, M. J., and X. Yu, 1999: Equatorial waves and the 1997–98 El Niño, *Geophys. Res. Lett.*, **26**, 2961–2964, doi:10.1029/1999GL004901.

Murray J., 1885: A summary of the scientific results. *Challenger Reports*, (1885), 1608 pp.

Nansen, F., 1900: The Norwegian north polar expedition, 1893-1896: Scientific results. ed. F. Nansen, Pub. by the Fridtjof Nansen fund for the advancement of science. Vol. 1–6.

Pedlosky, J., 1987: *Geophysical Fluid Dynamics*. Springer-Verlag, New York, 710 pp.

Pytkowicz, R. M., 1968: Water Masses and their Properties at 160°W in the Southern Ocean. *J. Oceanogr. Soc. Japan*, **24**, 1, 21–31.

Ridgway K. R., J. R. Dunn, and J. L. Wilkin, 2002: Ocean interpolation by four-dimensional least squares –Application to the waters around Australia. *J. Atmos. Ocean. Tech*., **19**, 1357–1375.

Roemmich, D., and J. Gilson, 2009: The 2004-2008 mean and annual cycle of temperature, salinity, and steric height in the global ocean from the Argo Program. *Prog. Oceanogr.*, **82,** 81-100.

Roemmich, D., G. C. Johnson, S. Riser, R. Davis, J. Gilson, W. B. Owens, S. L. Garzoli, C. Schmid, and M. Ignaszewski, 2009: The Argo Program: Observing the global ocean with profiling floats. *Oceanogr.*, **22**(**2**), 34–43, doi:10.5670/oceanog.2009.36.

Rudnick, D. L., and R. Ferrari, 1999: Compensation of horizontal temperature and salinity gradients in the ocean mixed layer. *Science*, **283**, 526–529.

Schmidtko, S., and G. C. Johnson, 2012: Multidecadal warming and shoaling of Antarctic Intermediate Water. *J. Climate*, **25**, 207–221, doi:10.1175/JCLI-D-11-00021.1.

Sethian, J. A., 1996: A fast marching level set method for monotonically advancing fronts. *Proc. Nat. Acad. Sci.*, **93**, 1591–1595.

Sethian, J. A., 1999: Fast Marching Methods. *SIAM Review,* **41**, 199–235.

Stommel, H., 1979: Determination of water mass properties of water pumped down from the Ekman layer to the geostrophic flow below. *Proc. Natl. Acad. Sci.,* **76**, 3051–3055.

Toole, J. M., R. A. Krishfield, M.-L. Timmermans, and A. Proshutinsky, 2011: The Ice-Tethered Profiler: Argo of the Arctic, *Oceanogr.,* **24**(**3**), 126–135, doi:10.5670/oceanog.2011.64.

Tsuchiya, M., L. D. Talley, and M. S. McCartney, 1994: Water-mass distributions in the western South Atlantic; A section from South Georgia Island (54S) northward across the equator. *J. Mar. Res.*, **52**, 55–81.

Wong, A. P. S., and G. C. Johnson, 2003: South Pacific Eastern Subtropical Mode water. *J. Phys. Oceanogr.*, **33**, 1493–1509, doi:10.1175/1520-0485(2003)033<1493:SPESMW>2.0.CO;2.

Wüst, G., and A. Defant, 1936: Schichtung und Zirkulation des Atlantischen Ozeans. *Wiss. Ergebn. Dt. Atlant. Exped. "Meteor" 1925–1927*, Bd. VI, Atlas, 103pp.

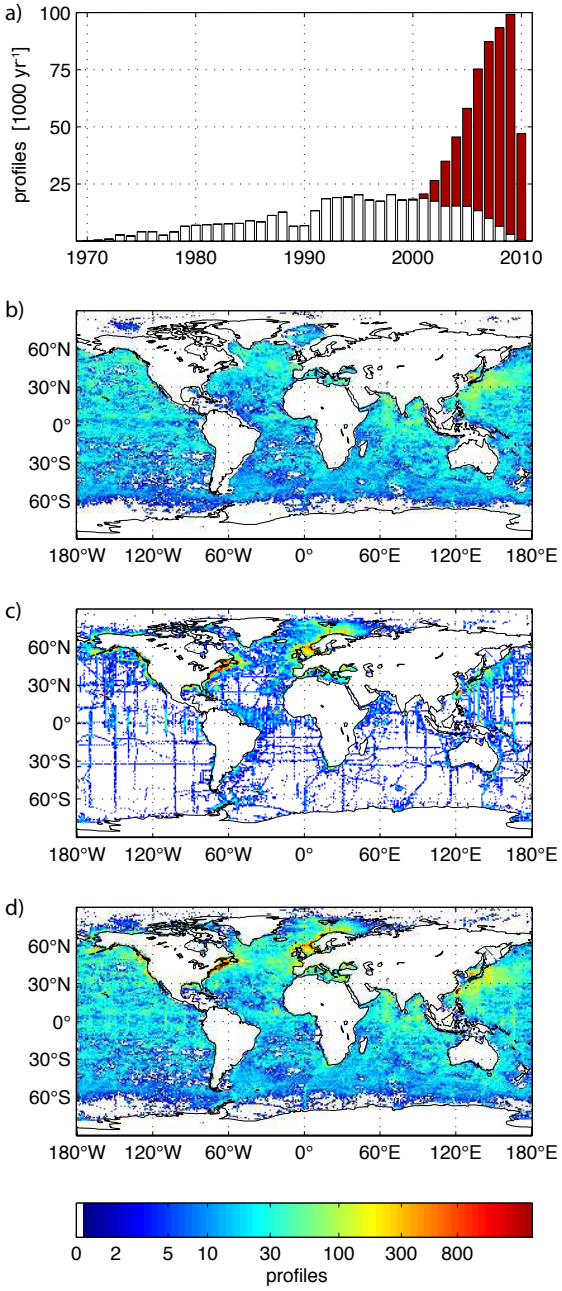

Figure 1. Data distribution for MIMOC. (a) Temporal distribution of WOD (white) and Argo/ITP profiles (red). (b) Spatial distribution of Argo and reduced ITP profiles (see text) for each 1°x1° grid box in logarithmic colors. (c) Similar to (b), but for WOD profiles. (d) Similar to (b), but for Argo, reduced ITP, and WOD profiles combined.

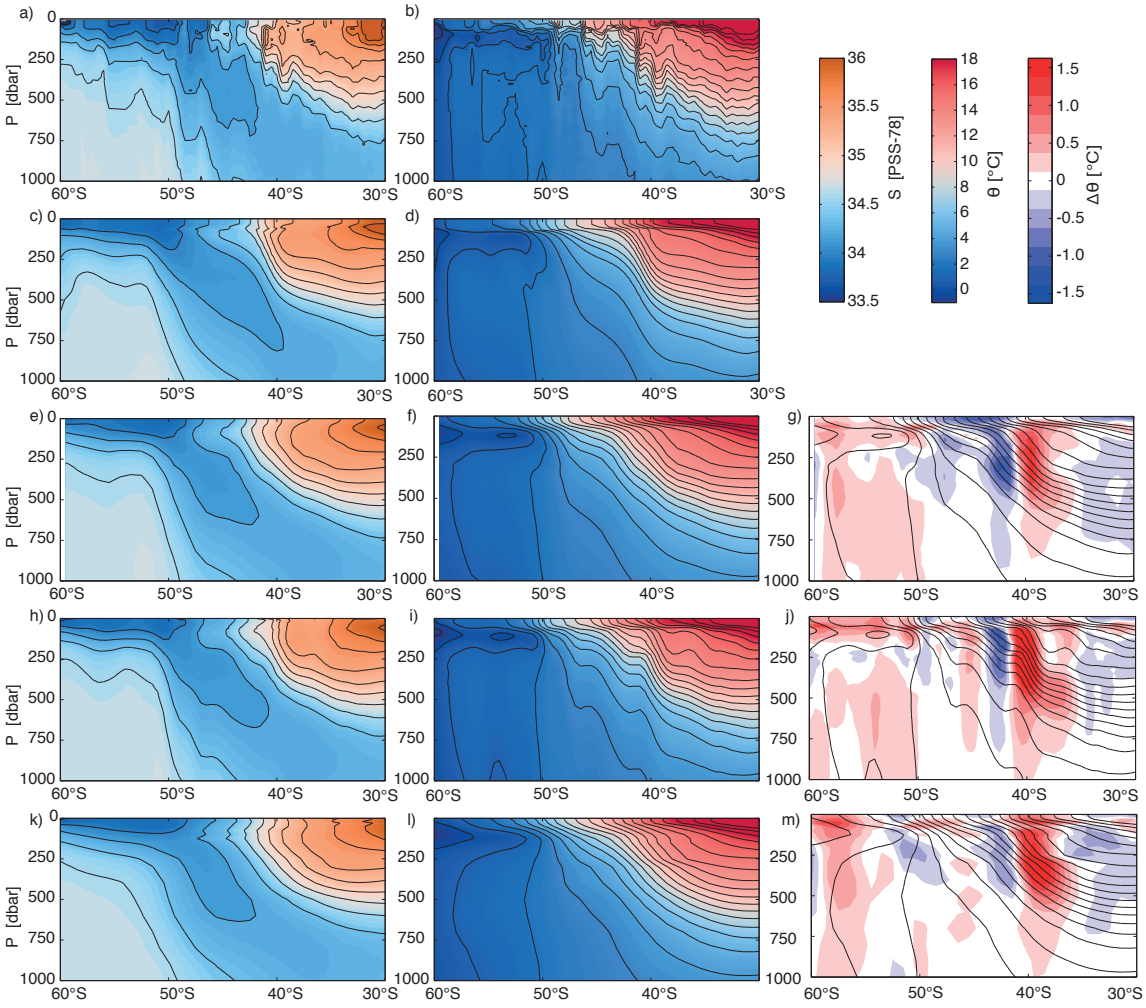

Figure 2. Meridional-vertical sections of (a) salinity (S) and (b) potential temperature (θ) for WOCE A16S in the western South Atlantic Ocean Jan.–Feb. 2005 (e.g., Johnson and Doney 2006). Corresponding MIMOC sections for (c–d) θ and S in January along 32.5°W. Similarly for (e–f) AMA and (g) MIMOC minus AMA θ (colors). Similarly for (h–j) CARS09 and (k–m) WOA09. Isohalines are contoured at 0.2 intervals and isotherms at 1°C intervals for each climatology and the synoptic data (black lines).

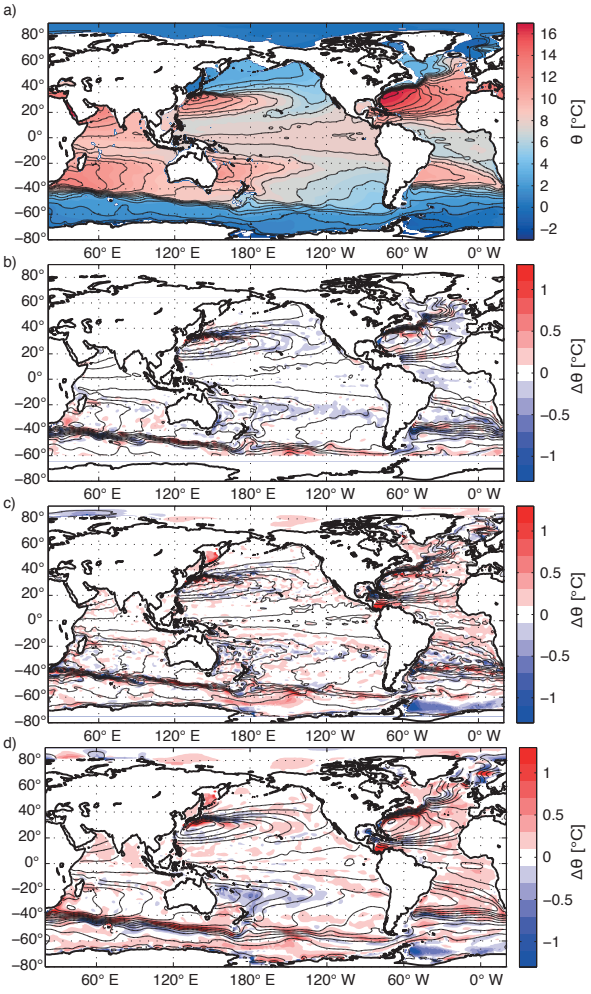

Figure 3. Maps of (a) MIMOC θ at 500 dbar in May and differences (MIMOC – each climatology) in color for (b) AMA, (c) CARS09, and (d) WOA09. Isotherms for each climatology are contoured at 1°C intervals (black lines).

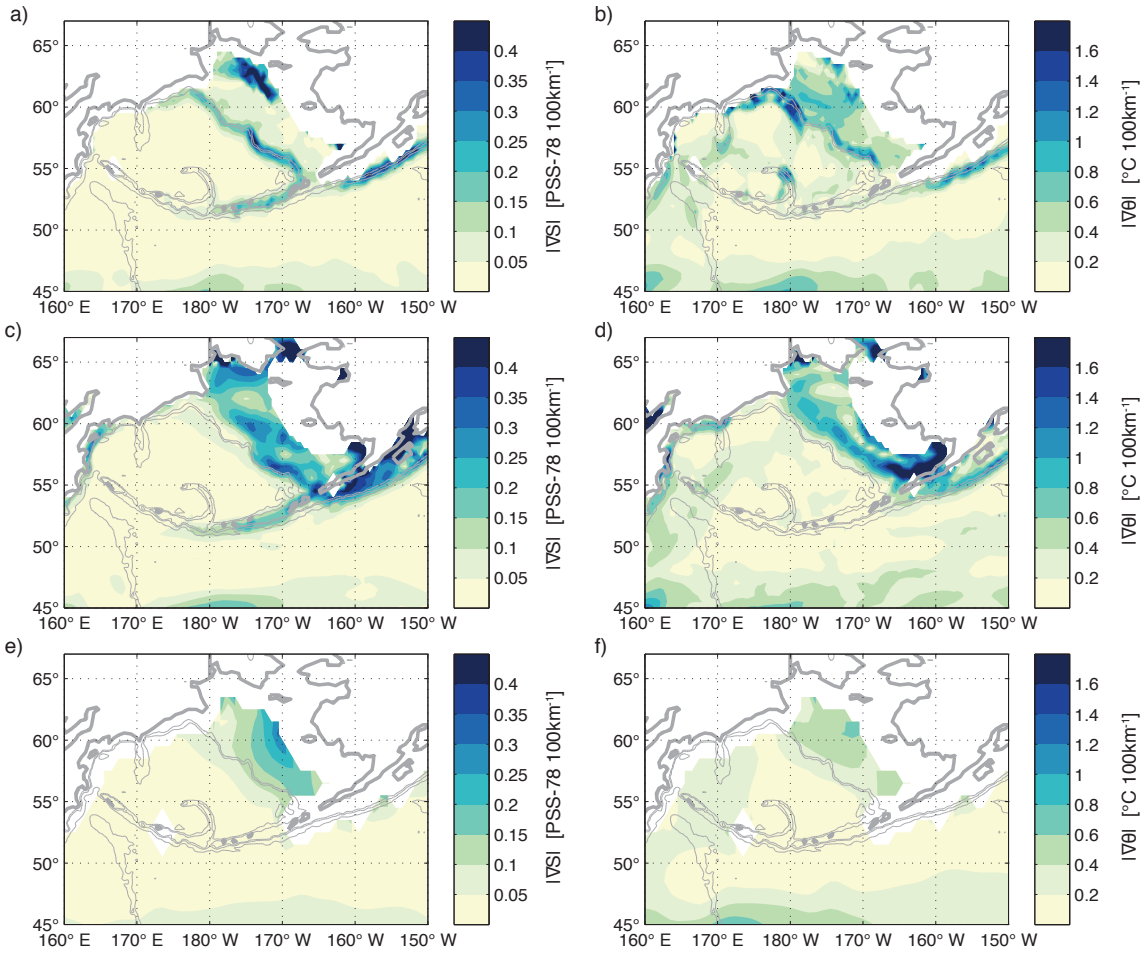

Figure 4. Maps of S (left panels) and θ (right panels) gradients at 50 dbar in the Bering Sea and Shelf for (a–b) MIMOC, (c–d) CARS09 (c-d), and (e–f) WOA09. The coast (thick grey lines) and 1000, 2000, and 3000-m isobaths (thin grey lines) are shown. The AMA climatology is omitted since it does not cover the Bering Sea or Shelf.

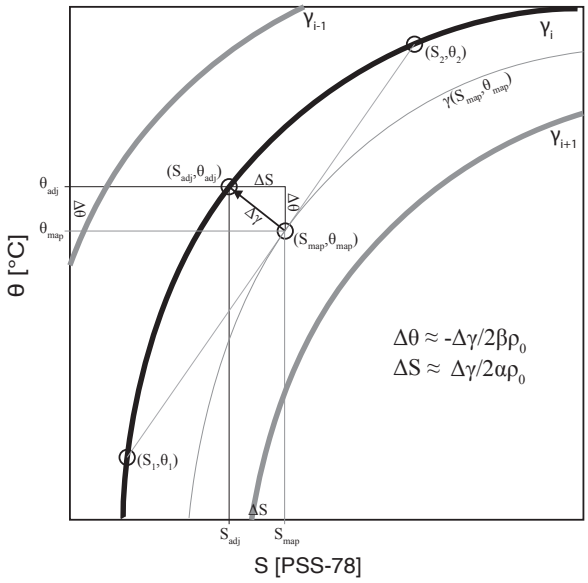

Figure 5. Schematic of artificial cabbeling in isopycnal mapping and its correction (see text for details). Points (S_1, θ_1) and (S_2, θ_2) represent raw data on an intital neutral surface γ_i, (S_{map}, θ_{map}) mapped values on a denser neutral surface, and (S_{adj} θ_{adj}) corrected/adjusted (and published) values back on the initial γ_i. The thermal expansion coeffient is α and the haline contraction coefficient is β.

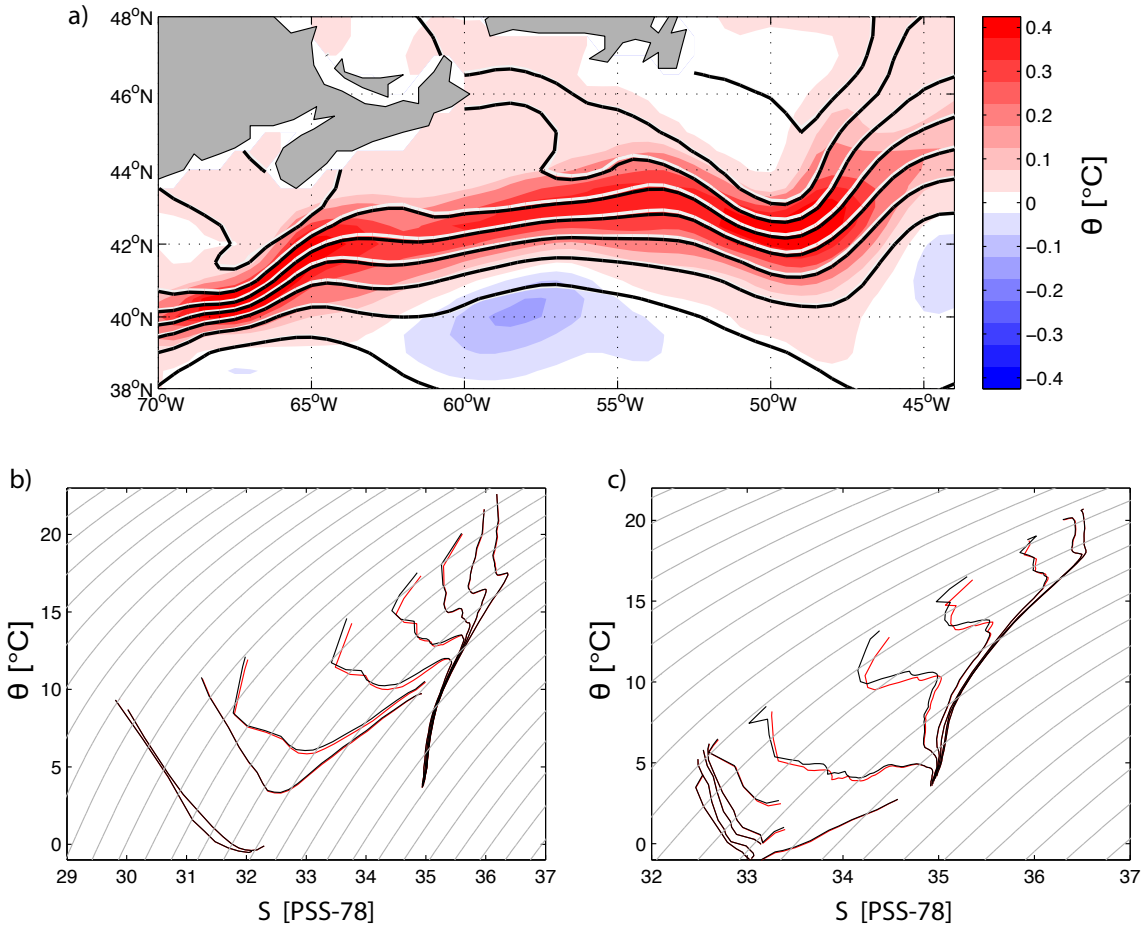

Figure 6. Map of (a) June potential temperature (θ) correction in mixed layer of the North Atlantic Current (color), isotherms contoured at 2°C intervals, in the (white) uncorrected and (black) corrected/adjusted data set. Sets of θ–S curves at 1° lat. intervals for June over the full (0-1500 dbar) depth at (b) 62.5°W and (c) 49.5°W showing uncorrected (red) and corrected (black) values.

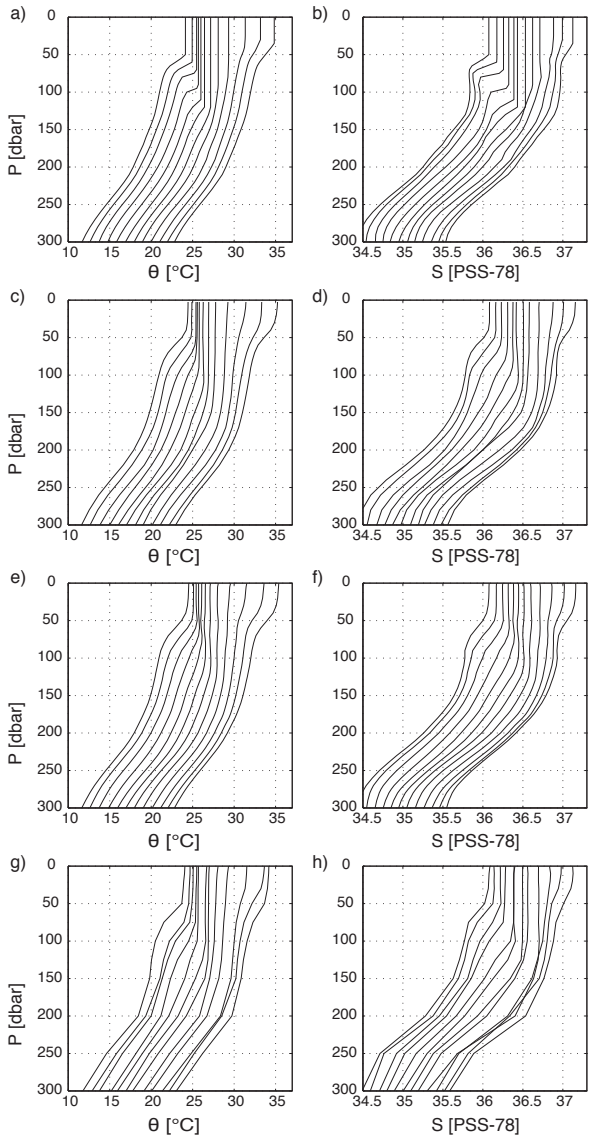

Figure 7. Temporal evolution over 12 months in the SEPSTMW formation region (20.5°S 99.5°W) starting with the lightest ML in March for (a) θ and (b) S in MIMOC offset by 1°C and 0.1 PSS-78 per month, respectively. Similarly for (c-d) AMA, (e–f) CARS09, and (g–h) WOA09.

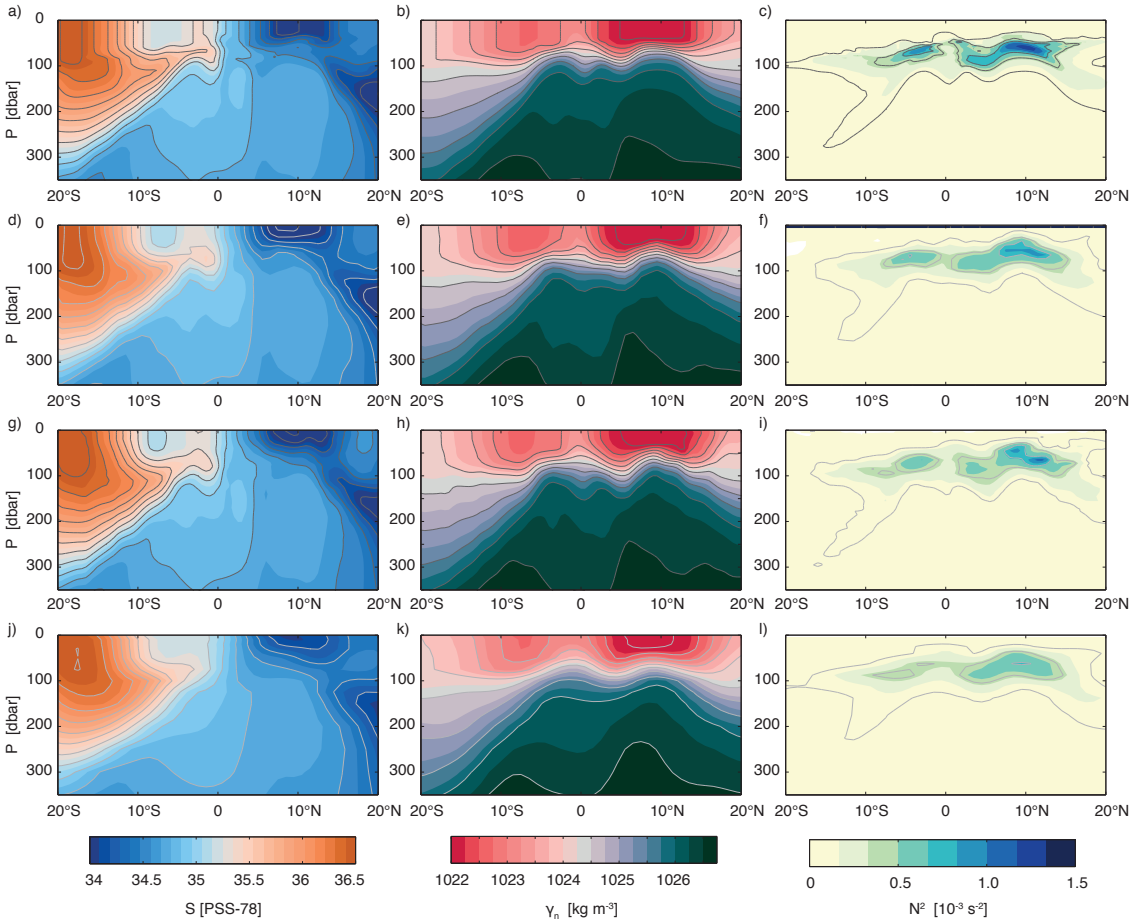

Figure 8. Meridional-vertical sections across the equatorial Pacific along 119.5°W in October, of S (left panels), γ_n, (central panels) and Brunt-Väisälä frequency squared, N^2, (right panels) for (a–c) MIMOC, (d–f) AMA, (g–i) CARS09, and (j–l) WOA09. Isohalines are contoured at 0.2 PSS-78 intervals, isopycnals at 0.5 kg m^{-3} intervals and isolines of N^2 at $0.3 \cdot 10^{-3}$ s^{-2} intervals starting at $0.1 \cdot 10^{-3}$ s^{-2}. AMA maps for individual Octobers have a stronger pycnocline than the multi-October average shown here.

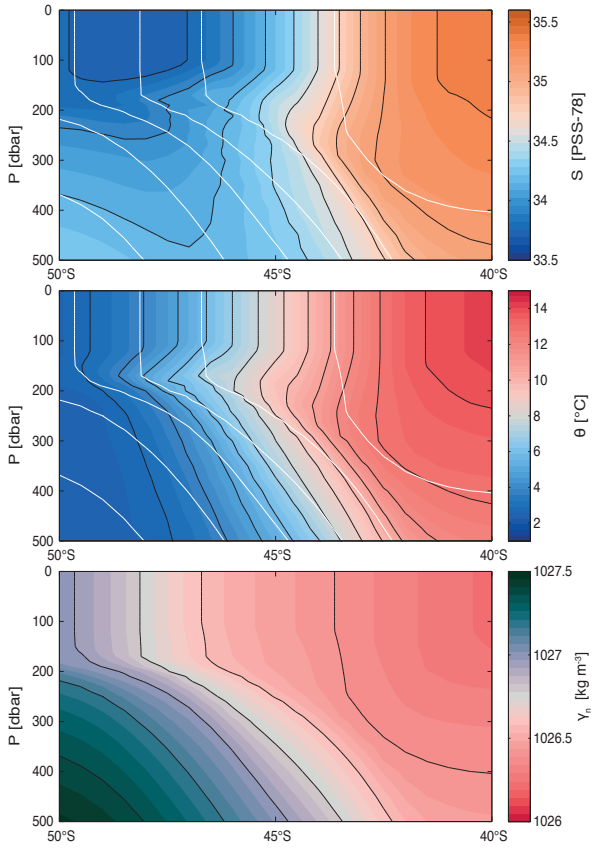

Figure 9. Meridional-vertical sections of MIMOC (a) S, (b) θ, and (c) γ_n along 60.5°E in September across the Antarctic Circumpolar Current. Isohalines are contoured at 0.2 PSS-78 intervals, isotherms at 1°C intervals in their respective panels (black lines) and isopycnals (white lines in (a) and (b), black lines in (c)) at 0.2 kg m^{-3} intervals.

TABLE 1. Parameters of climatologies compared in this study.

	Climatology name			
	WOA09	CARS09	AMA	MIMOC
Mapping surfaces	isobaric	isobaric	isobaric	isopycnal & mixed layer
Vertical level count (to 1500 dbar[1])	40 (24)	79 (60)	58 (53)	69 (69)[2]
Horizontal resolution	1°x1°	0.5°x0.5°	0.5°x0.5°	0.5°x0.5°
Max. depth (with seasonal cycle)	9000 m (1500 m)	5500 dbar (1800 dbar[3])	1975 dbar (1975 dbar)	1500 dbar (1500 dbar)
Mapping method	optimal interpolation	LOESS	optimal interpolation	optimal interpolation
Covariance shape, bathymetry influence on mapping	circular, regional boundaries between basins	CSIRO-BAR filter (ellipse along bathymetry)	distance penalty for profiles over varying topography	pathfinding algorithm using median filtered ETOPO-1
Mixed layer	none, separate climatology available	none, separate climatology available	none	included
Variables mapped	*T*, *S*, & biogeochemical	*T*, *S*, & limited biogeochemical	*T* & *S*	θ & *S*

[1]WOA09 uses depth for the vertical coordinate, so 1500 m is used as its break point.

[2]Also available for the mixed layer and on selected isopycnal surfaces.

[3]Mean, annual, and semi-annual harmonics from 0–1000 dbar, mean and annual harmonics from 1000-1800 dbar, mean only below 1800 dbar.